Journal of Membrane Science 499 (2016) 282–289

Contents lists available at ScienceDirect

Journal of Membrane Science

journal homepage: www.elsevier.com/locate/memsci

Membrane capacity and fouling mechanisms for ultrathin nanomembranes in dead-end filtration

J.D. Winans [a,1], K.J.P. Smith [a,1], T.R. Gaborski [b], J.A. Roussie [c], J.L. McGrath [a,*]

[a] Department of Biomedical Engineering, University of Rochester, Rochester, NY, United States
[b] Department of Biomedical Engineering, Rochester Institute of Technology, Rochester, NY, United States
[c] SiMPore, Henrietta, NY, United States

ARTICLE INFO

Article history:
Received 7 September 2015
Received in revised form
22 October 2015
Accepted 23 October 2015
Available online 27 October 2015

Keywords:
Fouling
Nanomembrane
Ultrafiltration
Capacity
Permeability

ABSTRACT

Ultrathin membrane technologies hold promise for improvements in membrane-based separation, however much remains to be learned about the ability of these membranes to support practical filtration processes. Here we examine the performance of new nanoporous silicon nitride (NPN) membranes in dead-end filtration using different methods for generating transmembrane pressure while varying nanoparticle types, sizes and concentrations. We infer membrane fouling by the amount of filtrate generated after a minute of dead-end filtration and show that each of these parameters has a strong influence on the rate of NPN fouling. Inverted centrifugation, which pulls large particles and aggregates away from the membrane as solvent passes through, increases filtrate volumes compared to forward centrifugation. Fitting filtration results to classic fouling models indicate that particles larger than the pores appear to foul membranes *via* cake formation at all concentrations, while filtration with particles much smaller than pores are impacted by pore obstruction before cake build up. Using direct comparisons in centrifuge devices, we show that NPN membranes have a comparable capacity to process suspensions of small colloids by dead end filtration at similar solvent speeds to thicker polycarbonate track-etched membranes, even with permeabilities more than two orders of magnitude higher.

1. Introduction

Ultrafiltration processes separate large and small solutes by forcing colloidal solutions through a nanoporous membrane sieve and have been part of industrial processes for decades [1]. The performance of an ultrafiltration membrane is often limited by fouling, which can occur either through physical pore interactions with the colloids or from a loss of permeability as colloids back up behind the filter. To minimize fouling, large-scale processes are often configured in a stirred cell or tangential flow filtration (TFF) device that sweeps foulant parallel to the membrane throughout the process. Studies have shown the importance of several parameters in the performance of ultrafiltration including species concentration [2,3], solution temperature [4], feed flow rate [5], stir speed [6], pH [7,8], particulate size [3,9], and membrane pore size [3].

In research laboratories, ultrafiltration is most commonly performed in benchtop centrifuges to concentrate samples, perform buffer exchanges, and separate colloids of significantly different sizes. Examples of samples prepared with benchtop centrifugation include proteins [10,11], nanoparticles [12–14], and pathogens [15–17]. Compared to TFF, dead-end ultrafiltration in a centrifuge is simpler, inexpensive, and less diluting of typical small-volume laboratory samples. Without a tangential component to the flow retained colloids can clog membranes quickly even at the laboratory scale and limit their utility.

As reviewed by Bacchin et al., considerable attention has been given in the literature to the investigation of the critical flux, where the flux in a tangential flow or dead-end filtration system is kept below some value so that the dispersive forces in the system will prevent the solute particles from condensing and depositing onto the membrane. At fluxes above this value a highly impermeable cake forms that dramatically decreases performance [18]. Across a variety of membrane types a transition from blockage models to cake filtration is observed after some time [19,20]. Generally, lower fluxes lead to less severe fouling [21–23], as the ameliorating effects of stirring or tangential flow have less of a concentration buildup against which to work. In the filtration of very small (1–100 nm) particles, Brownian back-diffusion is a significant driver of the dispersion of the local concentration

* Corresponding author.
E-mail address: jmcgrath@bme.rochester.edu (J.L. McGrath).
[1] Co-first-authors.

http://dx.doi.org/10.1016/j.memsci.2015.10.053
0376-7388/

increase at the surface of the membrane [24], especially in the absence of stirring or tangential flow.

Over the last decade, silicon manufacturing techniques have been used to create ultrathin (50 nm thick) nanoporous membranes [25,26]. While the recent development of lift-off methods are enabling ultrathin membrane sheets with areas greater than 100 cm^2 [27], the silicon-based chip remains the most common format for nanomembranes, with small sizes ($\sim$25 mm^2) that are suited to laboratory scale ($\sim$1 mL) filtration [26,28]. We have successfully integrated nanomembrane chips into custom-built centrifuge tubes and used the devices to measure the hydraulic permeability and sieving properties of nanomembranes [26]. These experiments have shown that nanomembranes exhibit a significant and expected increase in hydraulic permeability over conventional materials that are $\sim$10–1000$\times$ thicker [28]. Higher permeability alone is not sufficient to enable a membrane to be practically suited for ultrafiltration if its higher permeability is accompanied by a low *capacity* – a measure of the amount of material that can be processed by a membrane before it becomes useless from the effects of fouling [29]. Achieving high capacity is particularly challenging for nanomembranes because only a fraction of the chip area is permeable or 'active' while the rest is rendered impermeable by the silicon support structure.

In this work, we examine fouling and capacity of NPN membranes created using self-assembling pnc-Si [25] as a template. NPN membranes are more mechanically and chemically robust than pnc-Si while exhibiting similar flow and separation characteristics. Because we are interested in small-volume laboratory separations, we focused on the performance of NPN in a 1.5 mL centrifuge tube. We found that the particle type, size and concentration, and the configuration of the system all impacted the capacity of NPN. Particles larger (100 nm) than the pores (37 nm) clog membranes at concentrations three orders lower than particles much smaller (20 nm) than pores. Using a modified version of classic fouling models that account for the loss of head pressure during a centrifuge process, we analyzed temporal flow to determine the mechanisms of fouling for NPN. We found that both particle sizes eventually clog by cake formation but pore restriction can be seen prior to cake formation in the case of small particles. Finally we compared NPN to polycarbonate track-etched (TE) membranes with the same number of pores under identical operating conditions. We find that NPN membranes have a comparable capacity to TE membranes even with permeabilities more than two orders of magnitude higher, and argue that this is a direct result of their much thinner cross section.

2. Experimental

2.1. Nanomembrane fabrication

Complete details regarding membrane fabrication can be found in a previously published work [26]. In summary, a three layer stack of Si_xN_y, amorphous silicon (a-Si), and silicon dioxide (SiO_2) are deposited onto a 300 μm thick double-side-polished Si wafer which undergoes a rapid thermal anneal in order to crystalize the a-Si and form a pnc-Si film. The SiO_2 layer is removed and reactive ion etching in a Trion Minilok RIE transfers the pores into the Si_xN_y film. The pnc-Si mask is removed with a XeF_2 etch. The active membrane areas and chip edges are defined on the back side of the silicon wafer with standard lithography processes and etched using ethylene diamine pyrocatechol. Membranes are imaged in a transmission electron microscope (TEM) (Fig. 1a) and a pore distribution is calculated using custom image processing software (Fig. 1b).

2.2. Separations

Unless otherwise indicated, all separations were performed by assembling the filters into a custom 'SepCon' housing [26]. All SepCons were prewetted with 10 μL buffer on the top and bottom as a means of ensuring a thorough and continuous wetting of the inside of the pores. They were also prewetted as a means of reducing the possibility of antibodies adhering to a dry Si_xN_y surface and prematurely clogging the pores. Reverse centrifugation was performed by modifying both 1.5 mL conical centrifuge tubes and the SepCon assembly. The centrifuge tubes were filled with $\sim$0.5 mL of polydimethylsiloxane (PDMS). The PDMS served to eliminate 'dead volume' below the lowest point that the SepCon could reach in the centrifuge tube, which was just above the conical section. The SepCons were modified by cutting off the top portion of the reservoir that ordinarily rests on the top rim of the centrifuge tube. Removing the top section of the SepCon allows the remaining piece to slide lower than normally into the centrifuge tube, further reducing 'dead volume'. A Beckman Coulter Microfuge 18 centrifuge fitted with a F241.5P angled rotor was used for all centrifugations. All centrifuge separations in either the forward or reverse orientations were done at 3000 rpm (690*g*) unless otherwise noted. Filtrate volumes were determined by measuring the difference in mass of the conical centrifuge tube. Polycarbonate track etched membranes with pore sizes of 30 nm (PCT00313100) and 50 nm (PCT00513100) were purchased from Sterlitech. These membranes were fixed to the SepCon housing using PDMS. The PDMS fixative obscured a variable amount of the active area of each membrane, so a photo was taken of each of the cured membranes used for separations from which an effective

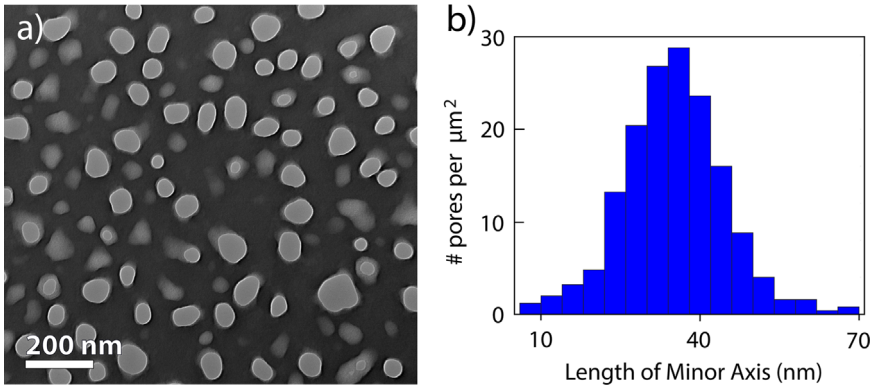

Fig. 1. NPN pore size distribution. a) A TEM image of a NPN nanomembrane. Circles with a rim are pores that span the thickness of the membrane, while gray patches are pits in the surface. b) A pore size histogram generated using image processing software shows that the average minor axis (the restricting axis) is $\sim$37 nm.

active area was calculated. Being hydrophilic, it was not necessary to wet the backside of these membranes. While separations using NPN membranes maintained a reservoir of ~10 μL on the backside of the membrane, track etched membranes emptied immediately into the bottom centrifuge vial, likely due to the differing hydrophobicities of the two membrane materials. Because of this, we compare the volume passed through wetted NPN and unwetted tracked etched membranes.

2.3. Materials

All water used for dilution purposes was UltraPure Distilled Water, purchased from Invitrogen life technologies. The phosphate buffered saline (pbs) solution was diluted from a 10×, pH 7.2 solution purchased from Gibco by life technologies. All colloids were diluted using a buffer of 1xPBS with 0.1% Tween 20. The Tween 20 (polyoxyethylene-sorbitan monolaurate) was purchased from Sigma. Both unlabeled and fluorescently labeled IgG were used in this study. The unlabeled IgG was from human serum, reagent grade, ≥95% (SDS-PAGE), essentially salt-free, lyophilized powder, purchased from Sigma-Aldrich. The fluorescently labeled goat anti-rabbit IgG (H+L) Antibody, Fluorescein (FITC) Conjugate, affinity purified, was purchased from Novex life technologies. The two antibodies were combined so that 2.5% were fluorescently labeled. The stock polystyrene NPs were carboxylate FluoSpheres, 2% solids, blue (365/415), in distilled wafer with 2 mM azide purchased from Invitrogen life technologies.

3. Results

We first measured the volume of filtrate collected as a function of time for particles smaller (20 nm) and larger (100 nm) than the pore sizes of the NPN membranes (~40 nm). All filters were prewetted before 300 μL of solution was added to the SepCon reservoir. The solutions were filtered using an angled centrifuge at 3000 rpm (690*g*). Fig. 2 plots total filtrate volume as a function of time for (a) 100 nm polystyrene NPs, (b) 20 nm polystyrene NPs and (c) IgG. Several concentrations were used for each of these three solutes. Concentrations for 100 nm NPs ranged from 10^9 up to 10^{13} parts/mL. 20 nm NPs ranged from 10^{11} to 10^{15}. IgG concentrations ranged from 2×10^{14} up to 2×10^{16} parts/mL (0.5–5 mg/mL). When spinning buffer only or working with low particle concentrations, the filtrate volume reached its maximum before the full 300 s (see Fig. 2a.) Because of geometric limits it was not possible to completely empty the SepCon reservoir and generally a volume of 250 μL and above is considered a completed filtration. All samples have their highest flux at the beginning of the separation, with filtrate volumes generally leveling off after 60 s. In part this is caused by a larger force acting on the initial volume which decreases as the fluid height diminishes. Additionally, there is very little particulate on the surface of the membrane at the outset and therefore buffer may flow freely. With time, some pores become partially or completely blocked with particles, while the rejected colloids begin to accumulate at the membrane surface to form a cake layer that reduces the effective permeability of the filter.

Examining the filtrate volume after 1 min of filtration (Fig. 3a), more clearly reveals the dependence of flux on particle concentration. While increasing particle concentration causes a more rapid flux decline in all cases, the flux is far more sensitive to low concentration of large particles. Because the 100 nm NPs are 2–3 times larger than the pores in the membrane, all of the particles will be rejected and contribute in some way to the cake layer. By comparison the 20 nm NPs are small enough to pass through the membrane, albeit with some hindrance and rejection. Below

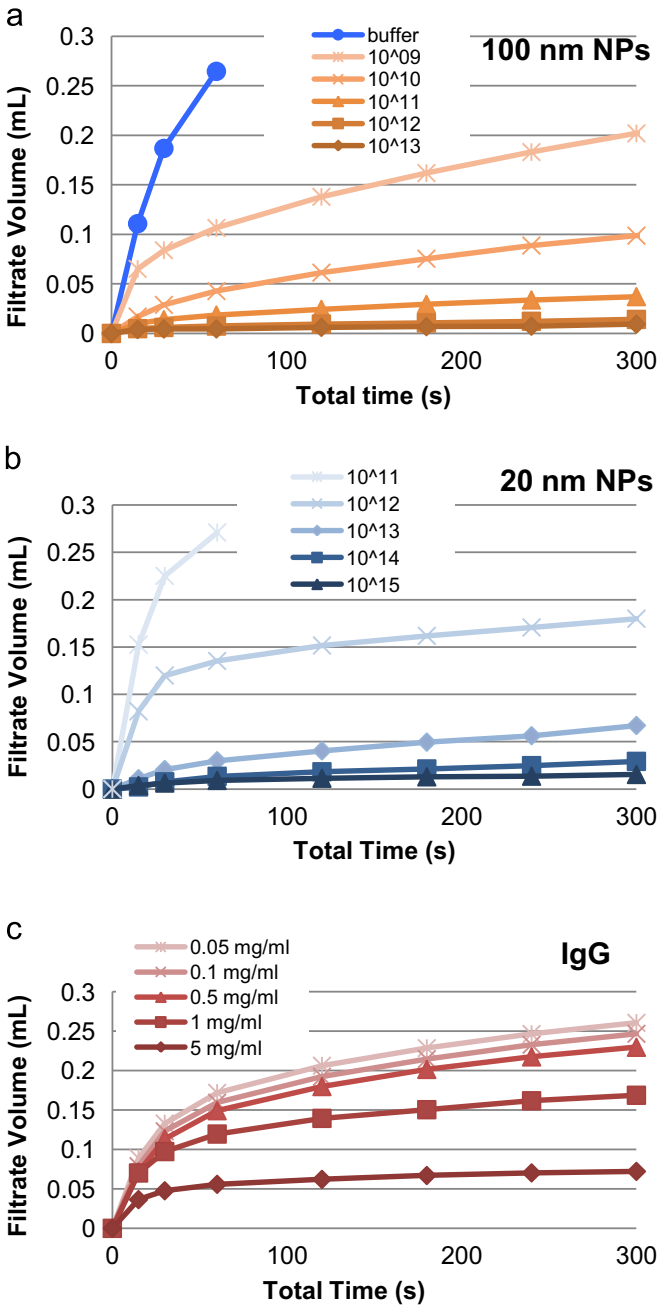

Fig. 2. Total filtrate volume as a function of time for various solutes and concentrations. a) Time progression for 100 nm polystyrene nanoparticles over a range of concentrations. b) Time progression for 20 nm polystyrene nanoparticles over a range of concentrations. c) Time progression for IgG over a range of concentrations. All three solutes have increased filtrate volume with decreased concentration. Comparing (a) and (b) shows that at the same concentration, solutions with 20 nm PS NPs flow faster than those with the larger 100 nm PS NPs.

10^{12} parts/mL, the entirety of the solution passes through the membrane after 1 min, while above this concentration there are enough particles rejected to detect a significant flux decline. At concentrations of 10^{13} and above the solutions act similar to the higher concentrations of 100 nm NPs with very rapid fouling in 1 min and low filtrate volumes. The solutions containing IgG showed a nearly linear decrease in filtrate volume after 1 min with increased concentration. This is most likely due to IgG being $14.5\times8.5\times4$ nm^3 in size [30] and therefore able to easily fit through the majority of the pores. In addition to forming a cake layer, fouling by IgG likely involves adsorption that shrinks the

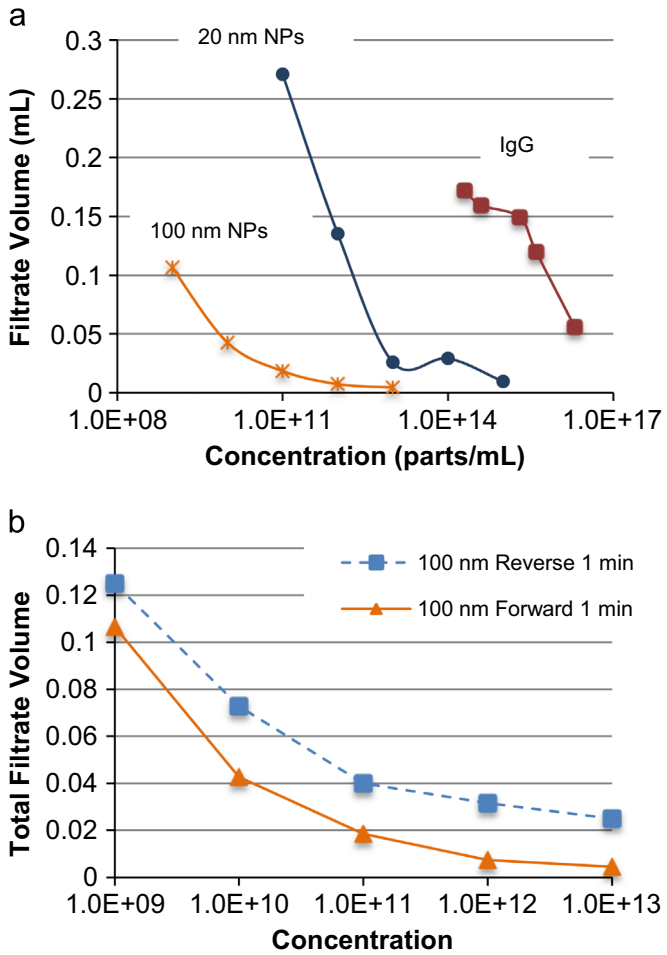

Fig. 3. : Parameters influencing filtrate volume. a) Total filtrate volumes for the three model solutes after 1 min of forward centrifugation. For each individual solute, increasing concentration results in decreased filtrate volume. b) Filtrate volume for identical solutions in either the forward or the reverse centrifuge direction. For all concentrations the reverse orientation provides higher filtrate volumes.

Si_xN_y membrane pores [25,31].

Inspired by commercial ultrafiltration systems that minimize membrane fouling by drawing filtrate through the membranes in a direction opposed to centrifugal forces (*e.g.* Millipore Centriprep), we compared filtrate volume *vs.* time for 100 nm polystyrene NPs in both 'forward' and 'reverse' orientations during centrifugation. The reverse centrifugations were performed using custom engineered centrifuge tubes that establish higher initial fluid levels outside of the central membrane cup (see Methods). For all concentrations examined, the reverse orientation displayed a greater total filtrate volume for the same spin time of 1 min (Fig. 3b). These results are consistent with the idea that a cake layer is responsible for reduced flux, and that a force acting to pull aggregated colloids away from the membrane enhances flux by reducing the size of this cake layer.

Scanning electron microscopy (SEM) was used to examine the nature of fouling on membrane surfaces in three different configurations. All experiments were done at 3000 RPM (690*g*) for 5 min with 100 nm PS NPs. Because nanomembranes are fabricated on the surface of a partially etched silicon substrate [25], it is possible to orient them in two ways relative to the flow. With the membrane side facing away from the flow, the particles will flow through the etched silicon 'trenches' in the substrate to the backside of the free-standing membrane. By contrast, with the membrane side facing the flow the particles will first see a flat surface with a permeable window before passing through the trench in the silicon substrate. These configurations are shown schematically on the left side of Fig. 4 along with the orientation of the centrifugal force for each experiment. Adjacent to these schematics are SEMs showing the side of the membrane facing the flow and illustrations giving our interpretation of NP build up. When flow enters the backside of the chip, we see a thick build-up (Fig. 4a) as the trenches act to funnel colloids onto the membrane surface. By contrast, with the chip configured in the same direction but the flow reversed (Fig. 4b), the particle layer is much thinner. Indeed, with individual particles visible in the film, the cake layer in this case appears to be only slightly larger than a monolayer. This result is consistent with the idea that the reverse orientation promotes flux by minimizing interaction between rejected particles and the membrane. This layer is notably mostly confined to the active membrane windows with a minimal 'spill-over' onto the impermeable areas outside the active membrane windows. This suggests that the Si_xN_y surface is largely resistant to NP absorption in the absence of external forces. A similar picture results when flow in the forward direction passes through the membrane side of the chip (Fig. 4c), except the layer appears thicker and a few more NPs remain bound to the membrane outside of the free-standing area.

Our data thus far indicate a primary role for cake formation in the fouling of NPN membranes. While this result is not surprising for a dead-end filtration process, we questioned if there was any evidence of a role for pore constriction or blockage. To examine this we incorporated classic mathematical models [32] of pore constriction, pore blockage, and cake filtration fouling mechanisms (Fig. 5a) into a model of centrifuge based dead-end filtration (see Supplement). We then conducted experiments over a range of PS NP concentrations and compared the evolution of flow to the predictions for these fouling mechanisms and for a case with no fouling (constant membrane resistance). For 100 nm PS particles (Fig. 5b), cake filtration gives a much better fit of the evolution of flow at all concentrations than either a pore constriction or constant membrane resistance model. A similar analysis of filtration with 20 nm particles (Fig. 5c) shows that a pore constriction model of fouling fits the data better at low concentrations (10^{11} and 10^{12}), while cake filtration better describes behavior at higher concentrations (10^{13} and 10^{14}). Interestingly, the fit for the 10^{12} concentration was significantly better for early times than later times, suggesting that the fouling mechanism changes during the time-course of the filtration. We examined this possibility more closely by fitting data to a hybrid model in which early times were described by pore constriction and later times by cake filtration (Fig. 5d) [19]. Assuming a sharp temporal transition between these modes of fouling, we found a local minimum in the root mean square error of the fit occurred at 60 s, and that the hybrid model does the best job of describing the filtration data with this chosen transition. A dramatic example of cake formation for 100 nm PS NPs is shown in the electron micrograph of Fig. 5e. Note the remarkable thinness of the membrane (~40 nm) compared to the thickness of the cake layer (1 μm) and even the size of individual NPs.

Since fouling can eventually render a membrane useless for filtration, an important metric is the membrane 'capacity' – a measure of the amount of sample that can be processed before the flux declines to impractical levels [29]. We sought to design an experiment that would reveal what advantage, if any, the thinness of our materials might have for improving capacity. We reasoned that a comparison to track etched membranes (TE) with a similar number and size of pores and otherwise identical operating conditions would isolate membrane thickness as a variable. Like nanomembranes, TE membranes contain discrete and well-defined pores that extend through the membrane thickness. Given that NPN membranes have only 5% of the chip area active, we sought

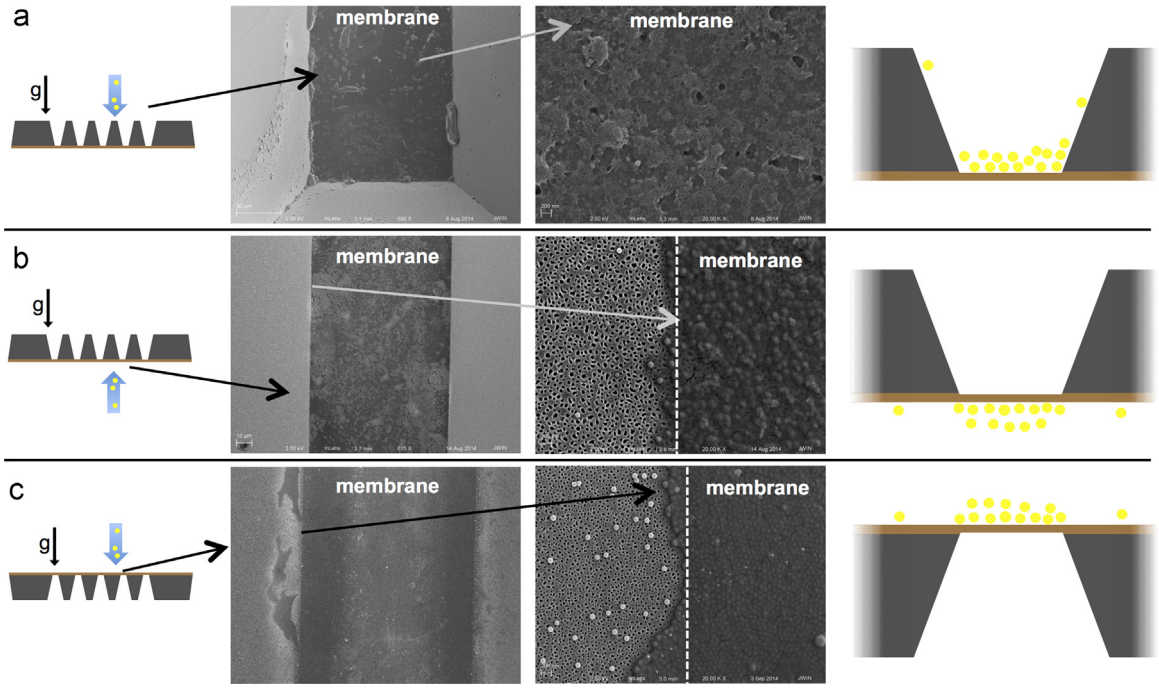

Fig. 4. : Buildup of 100 nm PS NP buildup on membranes under different chip and flow configurations. a) Forward centrifugation with NPs passing through silicon trenches first. b) Reverse centrifugation with NPs passing through the membrane first. c) Forward centrifugation with NPs passing through the membrane first. Note how NPs build up over the active area of the membrane in all cases while generally avoiding the impermeable silicon substrate areas.

TE membranes with 40 nm average pore sizes and 20 fold less porosity than our 15% porous NPN. We used commercially available TE membranes with either 30 nm or 50 nm pores with 6 pores/μm^2 [33] and respective porosities of 0.4% and 1%. For the purposes of this comparison we defined a capacity as the volume passed after the apparent hydraulic permeability of a membrane drops to 67% of its initial value in a centrifuge-based experiment with 20 nm PS NP. Defining the capacity with respect to intrinsic membrane permeability, rather than a flux, is necessary because the flux will decline as head height is lost in a centrifuge experiment.

The results shown in Fig. 6 show that NPN permeability starts significantly higher than both track etched membranes but falls dramatically over the first 50 μL passed. The permeability of both track etched membranes declines, but at a slower rate. This difference in behavior between NPN and TE can be explained as the higher initial permeability of NPN membranes resulting in a more rapid concentration polarization and cake formation. By contrast the low porosity and thick track etched membranes pass fluid so slowly that back diffusion can work to keep the concentration at the membrane surface down, enabling a more stable (but very low) permeability value. This relationship between the speed of filtration and membrane capacity is demonstrated for NPN membranes in Fig. 6b. By lowering the centrifuge speed from 2000 to 500 rpm, we find the capacity increases by 8 fold, becoming comparable to low flux TE membranes. Note that the permeability of the NPN membranes is always orders of magnitude higher than the TE membranes, even at capacity (Fig. 6b). These results strongly indicate that there is a tradeoff with high membrane permeability in dead-end filtration-under similar operating pressures, high permeability membranes tend to clog relatively more quickly and tend toward lower capacity. Thus, the intrinsic advantage of ultrathin membranes for separation and filtration processes may be in their ability to process practical quantities of fluids in short times at low pressures.

4. Discussion

Ultrathin silicon nanomembranes have been investigated as potential filtration devices since Tong et al. first drilled holes in a freestanding SiN membrane with a focused ion beam (FIB) [34]. FIB drilling is impractical for making more than a few dozen holes in a substrate, so other techniques have been used to generate sub-100 nm pores in sub-100 nm thick SiN films, including track etching [35] and using block-copolymer films as etching templates [36]. In 2007, Striemer et al. found that thin films of amorphous silicon can be treated to generate self-assembling nanopores in tuneable size distributions ranging from 5 to 80 nm, and with porosities of up to 35% [25]. Pnc-Si has since been used as a template to transfer pores into SiN films, which results in a more mechanically robust nanoporous nitride (NPN) membrane. The advent of atomically thin porous graphene represents the limiting case of the nanomembrane concept, but as yet these membranes have been limited to processing small volumes (<10 μL) and are still produced with laboratory-based manufacturing processes [37,38]. By contrast NPN is an ultrathin (<50 nm) membrane capable of processing practical laboratory sample volumes (100–500 μL) in the span of minutes with established pathways for industrially scaled and cost-effective manufacturing.

Ultrathin membranes represent an interesting departure from traditional polymeric membrane technology. A typical tortous-path polymeric membrane has ~ 100 μm^2 of internal surface area for every μm^2 of outer surface area, while for TE membranes this ratio is ~ 10 [33] and for SiN membranes it is ~ 0.1 [28]. This unique geometry means that transport across nanomembranes is dominated by surface phenomena. Indeed, a large role for surface phenomena has been seen in many of the application areas we have explored thus far. For example, we have previously shown that the rate of small molecule diffusion across an ultrathin membrane is limited by the time required to 'discover' an open pore rather than the time to diffuse through the pore [31,39]. Previous work by our lab has shown that a modified version of the classic Hagen–Poiseuille equation that accounts for pore entrance

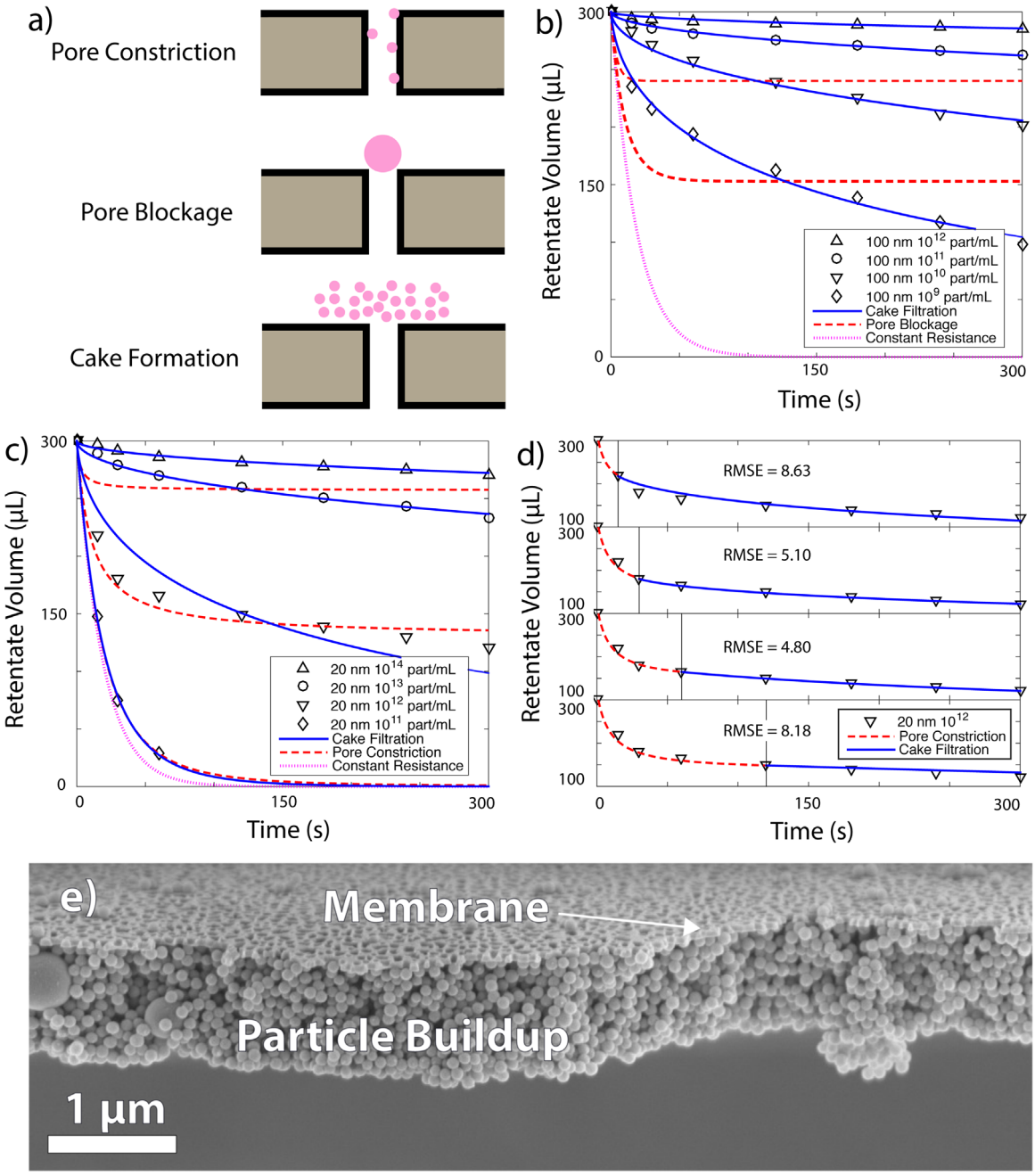

Fig. 5. : Mechanism of NPN fouling. a) The fouling mechanisms modeled. Pore blockage can occur when particles are larger than the pores, while pore constriction is expected when particles are smaller than the pores. Cake filtration can happen with particles of any size. b) Plots showing retentate volume as a function of time with centrifugation using 100 nm nanoparticles indicates that cake filtration dominates the flux characteristics for all concentrations studied. c) Fitting retentate volume *vs.* time for separations for various concentrations of 20 nm nanoparticles. Data is fit using classic flux decline models describing pore constriction and cake filtration modes of fouling. d) Picking four different transition points in the 10^{12} data and fitting the data prior to the transition using pore constriction and after the transition using cake filtration reveals a local minimum in the root mean square error, suggesting the process switches fouling modes at around 60 s. e) A TEM image of cake formation. Solvent was passed from the bottom of the membrane to the top, and the particles, which are larger than the pores, were held back, forming a dense cake layer.

and exit resistances [40] is an excellent predictor of pressure-driven hydraulic flux through the membrane [28]. Similarly, our analysis of pnc-Si nanomembranes as electro-osmotic pumps indicates that a transmembrane electric field is most accurately modeled by accounting for entrance and exit resistances that reduce the transmembrane electric field for a given applied voltage [41]. Given the dominant role for surface phenomena in transport through ultrathin membranes, and the limited opportunity for internal fouling, it is not surprising that cake filtration is the dominant fouling mechanism for dead-end filtration with NPN.

Another unique aspect of chip-based membranes like NPN is a structure in which membrane 'windows' span across trenches etched in solid silicon substrates. While such membrane chips have been used for a variety of nanofabricated membrane materials [38,42] our work is the first to examine the relationship between chip-based membrane orientation and and flow direction in dead end filtration. We found that upstream-facing trenches act to funnel colloids to the membrane surface and enhance cake formation. We further found that cake formation was diminished, and flux increased, when the flow was antiparallel to the direction of the centrifugal force ('reverse centrifugation'). Thus the ideal configuration for dead end centrifugation appears to be one in

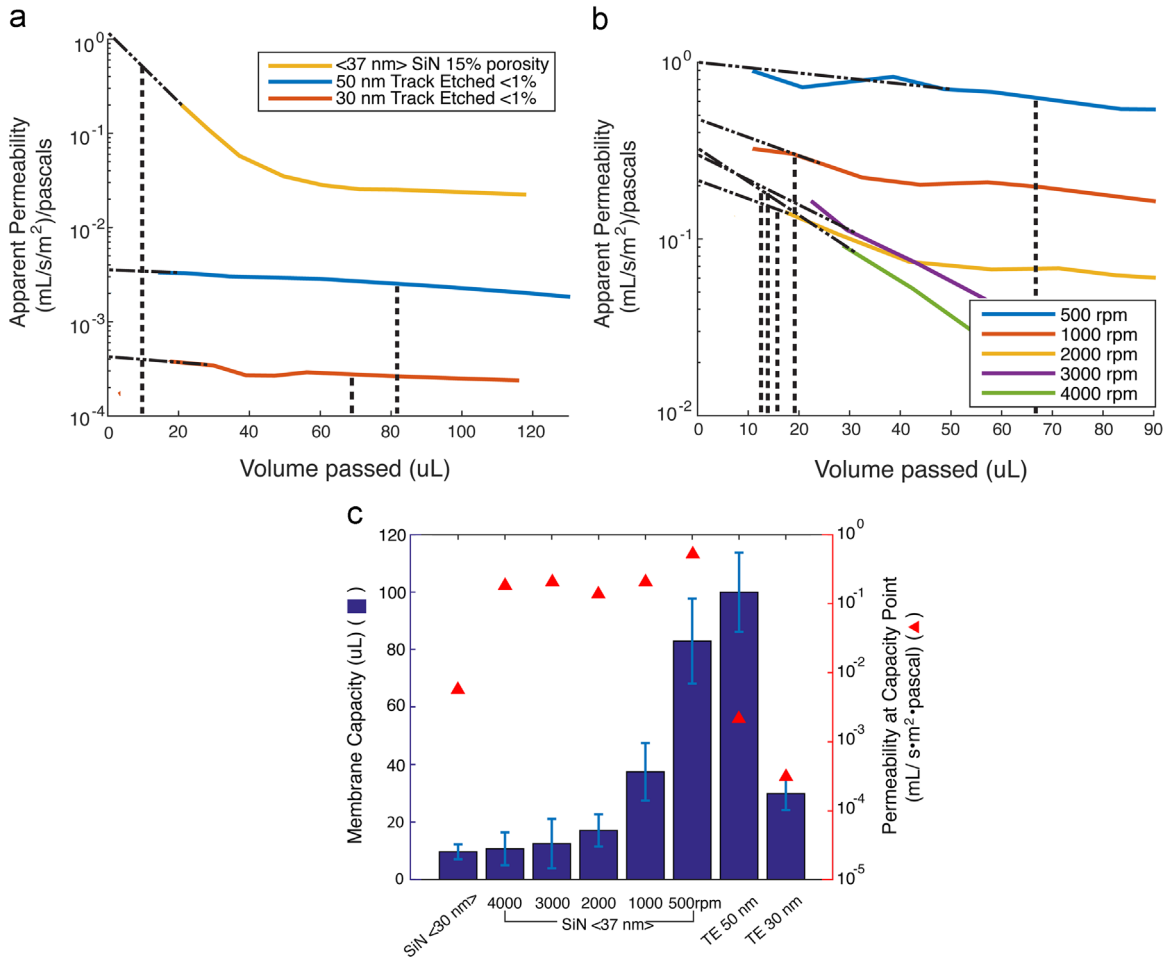

Fig. 6. : Capacity of NPN vs. TE membranes. a) Filtrate volume vs. apparent permeability for two different track etched membranes (6 μm thick) and an NPN membrane (~50 nm thick). Note the log vertical axis is needed to place TE and NPN membranes on the same graph. Because of the thinness of the NPN membranes, separations using them happen faster, meaning that more particles build up behind the membrane and cause cake layer formation to dominate the hydraulic permeability, whereas the significantly lower flux of track etched membranes (due to lower porosities and thicker membranes) causes separations to happen slower, leading to higher capacities. Dashed vertical lines represent the volume at which permeability of a membrane has fallen to 67% of its estimated initial flux (dash–dot–dash lines), a value we term the capacity of the membrane. b) NPN membranes with 37 nm pore sizes and 15% porosity were spun at several different speeds. As expected, hydraulic permeability was highest at the lowest spin speeds, due to the decreased concentration of particles at the membrane surface. Data collected before 10 μL had passed was ignored due to variations in backside dead volume wetting. c) Relative capacities for the four membranes (and the four spin speeds for the $<37\ \mathrm{nm}>$ membranes) as well as the permeability at the capacity point (red triangles) are illustrated. At 500 rpm, NPN membranes have permeabilities more than two orders of magnitude greater than 50 nm track etched membranes, but the capacities of the membranes are comparable. Error bars are $+/-$ one standard deviation as calculated from the goodness of fits of the dotted lines (dash–dot–dot) in Fig. 6a and b. All separations in this figure were performed with 20 nm PS NPs at a concentration of 10^{12} particles/mL. (For interpretation of the references to color in this figure legend, the reader is referred to the web version of this article.)

which the membrane faces upstream of a reversed flow field. Because the assemblies for reverse configurations required awkward modifications of devices designed for forward centrifugation, the bulk of the experiments here were done in a 'forward' configuration (Fig. 4a). We are in the process of designing special housings to enable easier investigation of reverse centrifugation.

Finally, our work illustrates a tradeoff between hydraulic permeability and membrane capacity important for the application of ultrathin membranes. Under otherwise identical conditions (transmembrane pressure, pore size and number) TE membranes that were $>100\times$ thicker than NPN displayed a higher capacity. This can be understood by the fact that a high membrane permeability results in a more rapid build up of rejected colloids leading to concentration polarization and cake filtration. By contrast low permeability TE membranes operate slow enough that particle diffusion away from the membrane can act to slow the growth of a concentration polarization layer at the membrane. Consistent with this explanation, the capacity of NPN membranes became comparable to that of TE membranes as the transmembrane pressure was lowered. The results suggest that the benefits of ultrathin membranes such as NPN may be in their ability to process practical quantities of fluids at lower pressures. Lower pressure requirements in turn should result in lower energy use and lower costs. The current chip formats may benefit the design of microfluidic systems because filtration components can be incorporated without significantly increasing the overall system pressure requirements. With the advent of lift-off techniques that create large sheets (~100 cm^2) of active ultrathin membrane [27], larger format applications such as bioprocessing may eventually benefit from the ability to operate effectively at lower pressures.

Acknowledgments

The authors would like to thank Brian McIntyre and URnano for help with material deposition and electron microscopy. This work was funded by the National Science Foundation, GOALI #1159579. A corporate start-up, SiMPore Inc., participated in this work. SiMPore is working to commercialize the NPN membrane material used in the study. J.M. and T.G are founders of SiMPore. J.R. was

employed by SiMPore during this project.

Appendix A. Supplementary material

Supplementary data associated with this article can be found in the online version at doi:10.1016/j.memsci.2015.10.053.

References

[1] M. Cheryan, Ultrafiltration Handbook, Technomic Pub. Co., Lancaster, Pa. (1986), p. 375.
[2] J.E. Flinn, Membrane Science and Technology; Industrial, Biological, and Waste Treatment Processes, Plenum Press, New York (1970), p. 234 , Battelle Memorial Institute. Columbus Laboratories.
[3] P.A. Schweitzer, Handbook of Separation Techniques for Chemical Engineers, McGraw-Hill, New York (1979), p. 1200 , in various pagings.
[4] D.J. Nichols, M. Cheryan, Production of soy isolates by ultrafiltration-process engineering characteristics of the hollow fiber system, J. Food Process. Preserv. 5 (2) (1981) 103–118.
[5] B.H. Chiang, M. Cheryan, Ultrafiltration of skimmilk in hollow fibers, J. Food Sci. 51 (2) (1986) 340–344.
[6] S. Das, P. Saha, G. Pugazhenthi, Modeling and simulation of stirred dead end ultrafiltration process using the aspen engineering suite, Ind. Eng. Chem. Res. 48 (9) (2009) 4428–4439.
[7] J.F. Hayes, et al., Studies on whey processing by ultrafiltration. 2. Improving permeation rates by preventing fouling, Aust. J. Dairy Technol. 29 (3) (1974) 132–140.
[8] S.H. Lin, C.L. Hung, R.S. Juang, Effect of operating parameters on the separation of proteins in aqueous solutions by dead-end ultrafiltration, Desalination 234 (1–3) (2008) 116–125.
[9] U. Merin, M. Cheryan, Factors affecting the mechanism of flux decline during ultrafiltration of cottage cheese whey, J. Food Process. Preserv. 4 (3) (1980) 183–198.
[10] E. Rosenberg, et al., Ultrafiltration concentration of monoclonal antibody solutions: development of an optimized method minimizing aggregation, J. Membr. Sci. 342 (1–2) (2009) 50–59.
[11] M. Feins, K.K. Sirkar, Highly selective membranes in protein ultrafiltration, Biotechnol. Bioeng. 86 (6) (2004) 603–611.
[12] A. Bruneau, et al., Size distribution effects of cadmium tellurium quantum dots (CdS/CdTe) immunotoxicity on aquatic organisms, Environ. Sci. Process. Impacts 15 (3) (2013) 596–607.
[13] F. Springer, S. Laborie, C. Guigui, Removal of SiO_2 nanoparticles from industry wastewaters and subsurface waters by ultrafiltration: investigation of process efficiency, deposit properties and fouling mechanism, Sep. Purif. Technol. 108 (2013) 6–14.
[14] J. Lohwacharin, S. Takizawa, Effects of nanoparticles on the ultrafiltration of surface water, J. Membr. Sci. 326 (2) (2009) 354–362.
[15] S.D. Leskinen, V.J. Harwood, D.V. Lim, Rapid dead-end ultrafiltration concentration and biosensor detection of enterococci from beach waters of Southern California, J. Water Health 7 (4) (2009) 674–684.
[16] E. Arkhangelsky, V. Gitis, Effect of transmembrane pressure on rejection of viruses by ultrafiltration membranes, Sep. Purif. Technol. 62 (3) (2008) 619–628.
[17] R. van Reis, A. Zydney, Membrane separations in biotechnology, Curr. Opin. Biotechnol. 12 (2) (2001) 208–211.
[18] P. Bacchin, P. Aimar, R.W. Field, Critical and sustainable fluxes: theory, experiments and applications, J. Membr. Sci. 281 (1–2) (2006) 42–69.
[19] C.-C. Ho, A.L. Zydney, A combined pore blockage and cake filtration model for protein fouling during microfiltration, J. Colloid Interface Sci. 232 (2) (2000) 389–399.
[20] K.-J. Hwang, C.-Y. Liao, K.-L. Tung, Analysis of particle fouling during microfiltration by use of blocking models, J. Membr. Sci. 287 (2) (2007) 287–293.
[21] S. Kuiper, et al., Development and applications of very high flux microfiltration membranes, J. Membr. Sci. 150 (1) (1998) 1–8.
[22] K.J. Kim, V. Chen, A.G. Fane, Some factors determining protein aggregation during ultrafiltration, Biotechnol. Bioeng. 42 (2) (1993) 260–265.
[23] W.R. Bowen, Q. Gan, Properties of microfiltration membranes: adsorption of bovine serum albumin at polyvinylidene fluoride membranes, J. Colloid Interface Sci. 144 (1) (1991) 254–262.
[24] V. Chen, et al., Particle deposition during membrane filtration of colloids: transition between concentration polarization and cake formation, J. Membr. Sci. 125 (1) (1997) 109–122.
[25] C.C. Striemer, et al., Charge- and size-based separation of macromolecules using ultrathin silicon membranes, Nature 445 (7129) (2007) 749–753.
[26] J.P.S. DesOrmeaux, et al., Nanoporous silicon nitride membranes fabricated from porous nanocrystalline silicon templates, Nanoscale 6 (18) (2014) 10798–10805.
[27] J.M. Joshua, et al., Lift-off of large-scale ultrathin nanomembranes, J. Micromech. Microeng. 25 (1) (2015) 015011.
[28] T.R. Gaborski, et al., High-performance separation of nanoparticles with ultrathin porous nanocrystalline silicon membranes, ACS Nano 4 (11) (2010) 6973–6981.
[29] A.L. Zydney, C.C. Ho, Effect of membrane morphology on system capacity during normal flow microfiltration, Biotechnol. Bioeng. 83 (5) (2003) 537–543.
[30] Y.H. Tan, et al., A nanoengineering approach for investigation and regulation of protein immobilization, ACS Nano 2 (11) (2008) 2374–2384.
[31] J.L. Snyder, et al., An experimental and theoretical analysis of molecular separations by diffusion through ultrathin nanoporous membranes, J. Membr. Sci. 369 (1–2) (2011) 119–129.
[32] R. van Reis, A. Zydney, Bioprocess membrane technology, J. Membr. Sci. 297 (1–2) (2007) 16–50.
[33] Corporation, S., PCTE Product and Performance Characteristics. 2015; Available from: ⟨http://www.sterlitech.com/pcte-product-and-performance-characteristics.html⟩.
[34] H.D. Tong, et al., Silicon nitride nanosieve membrane, Nano Lett. 4 (2) (2004) 283–287.
[35] W.M. Zhang, et al., Fabrication of nanoporous silicon dioxide/silicon nitride membranes using etched ion track technique, Nucl. Instrum. Methods Phys. Res. Sect. B: Beam Interact. Mater. At. 266 (12–13) (2008) 3166–3169.
[36] F. Montagne, et al., Molecular transport through nanoporous silicon nitride membranes produced from self-assembling block copolymers, Nanoscale 4 (19) (2012) 5880–5886.
[37] K. Celebi, et al., Ultimate permeation across atomically thin porous graphene, Science 344 (6181) (2014) 289–292.
[38] S.P. Surwade, et al., Water desalination using nanoporous single-layer graphene, Nat. Nano 10 (5) (2015) 459–464.
[39] R. Ishimatsu, et al., Ion-selective permeability of an ultrathin nanoporous silicon membrane as probed by scanning electrochemical microscopy using micropipet-supported ITIES tips, Anal. Chem. 82 (17) (2010) 7127–7134.
[40] Z. Dagan, S. Weinbaum, R. Pfeffer, An infinite-series solution for the creeping motion through an orifice of finite length, J. Fluid Mech. 115 (1982) 505–523.
[41] J. Getpreecharsawas, J.L. McGrath, D.A. Borkholder, The electric field strength in orifice-like nanopores of ultrathin membranes, Nanotechnology 26 (4) (2015) 045704.
[42] E.E. Nuxoll, et al., Composite block polymer-microfabricated silicon nanoporous membrane, ACS Appl. Mater. Interfaces 1 (4) (2009) 888–893.